

# Functionalized block co-polymer pro-drug nanoparticles with anti-cancer efficacy in 3D spheroids and in an orthotopic triple negative breast cancer model

Taresco, Vincenzo; Abelha, Thais F.; Cavanagh, Robert J.; Vasey, Catherine E.; Anane-Adjei, Akosua B.; Pearce, Amanda K.; Monteiro, Patrícia F.; Spriggs, Keith A.; Clarke, Philip; Ritchie, Alison; Martin, Stewart; Rahman, Ruman; Grabowska, Anna M.; Ashford, Marianne B.; Alexander, Cameron

DOI:

[10.1002/adtp.202000103](https://doi.org/10.1002/adtp.202000103)

License:

Creative Commons: Attribution (CC BY)

*Document Version*

Publisher's PDF, also known as Version of record

*Citation for published version (Harvard):*

Taresco, V, Abelha, TF, Cavanagh, RJ, Vasey, CE, Anane-Adjei, AB, Pearce, AK, Monteiro, PF, Spriggs, KA, Clarke, P, Ritchie, A, Martin, S, Rahman, R, Grabowska, AM, Ashford, MB & Alexander, C 2021, 'Functionalized block co-polymer pro-drug nanoparticles with anti-cancer efficacy in 3D spheroids and in an orthotopic triple negative breast cancer model', *Advanced Therapeutics*, vol. 4, no. 1, 2000103.  
<https://doi.org/10.1002/adtp.202000103>

[Link to publication on Research at Birmingham portal](#)

## General rights

Unless a licence is specified above, all rights (including copyright and moral rights) in this document are retained by the authors and/or the copyright holders. The express permission of the copyright holder must be obtained for any use of this material other than for purposes permitted by law.

- Users may freely distribute the URL that is used to identify this publication.
- Users may download and/or print one copy of the publication from the University of Birmingham research portal for the purpose of private study or non-commercial research.
- User may use extracts from the document in line with the concept of 'fair dealing' under the Copyright, Designs and Patents Act 1988 (?)
- Users may not further distribute the material nor use it for the purposes of commercial gain.

Where a licence is displayed above, please note the terms and conditions of the licence govern your use of this document.

When citing, please reference the published version.

## Take down policy

While the University of Birmingham exercises care and attention in making items available there are rare occasions when an item has been uploaded in error or has been deemed to be commercially or otherwise sensitive.

If you believe that this is the case for this document, please contact [UBIRA@lists.bham.ac.uk](mailto:UBIRA@lists.bham.ac.uk) providing details and we will remove access to the work immediately and investigate.

Download date: 19. Apr. 2024

# Functionalized Block Co-Polymer Pro-Drug Nanoparticles with Anti-Cancer Efficacy in 3D Spheroids and in an Orthotopic Triple Negative Breast Cancer Model

Vincenzo Taresco, Thais F. Abelha, Robert J. Cavanagh, Catherine E. Vasey, Akosua B. Anane-Adjei, Amanda K. Pearce, Patrícia F. Monteiro, Keith A. Spriggs, Philip Clarke, Alison Ritchie, Stewart Martin, Ruman Rahman, Anna M. Grabowska, Marianne B. Ashford, and Cameron Alexander\*


Amphiphilic block co-polymers composed of poly(ethylene glycol)-co-poly(lactide)-co-poly(2-((*tert*-butoxycarbonyl)amino)-3-propyl carbonate) (PEG-pLA-pTBPC) are synthesized in monomer ratios and arrangements to enable assembly into nanoparticles with different sizes and architectures. These materials are based on components in clinical use, or known to be biodegradable, and retain the same fundamental chemistry across “AB” and “BAB” block architectures. In MCF7 and MDA-MB-231 breast cancer cells, nanoparticles of <100 nm are internalized most rapidly, by both clathrin- and caveolin-mediated pathways. In THP-1 cells, polymer architecture and length of the hydrophilic block is the most important factor in the rate of internalization. The organ distributions of systemically injected nanoparticles in healthy mice indicate highest accumulation of the BAB-blocks in lungs and liver and the lowest accumulation in these organs of a methoxyPEG<sub>5000</sub>-pLA-pTBPC polymer. Conjugation of doxorubicin via a serum-stable urea linker to the carbonate regions of PEG<sub>5000</sub>-pLA-pTBPC generates self-assembling nanoparticles which are more cytotoxic in 2D, and penetrate further in 3D spheroids of triple negative breast cancer cells, than the free drug. In an aggressive orthotopic triple negative breast cancer mouse model, the methoxyPEG<sub>5000</sub>-pLA-pTBPC is of similar potency to free doxorubicin but with no evidence of adverse effects in terms of body weight.

## 1. Introduction

Polymer pro-drugs offer much promise for drug delivery, owing to the ability to tune the macromolecular structures for solubility and stability in biological fluids, and to encode for drug release in disease-specific environments.<sup>[1]</sup> In addition, the wide variety of synthetic routes available for constructing polymers is allowing materials with highly defined structures, architectures and release mechanisms to be formed from easily accessible precursors.<sup>[2]</sup> Accordingly, it is now possible to construct new materials with a large range of physico-chemical properties and, of significant importance, from building blocks which are either already in clinical use,<sup>[3]</sup> or which have relatively low barriers to translation.<sup>[4]</sup> However, for diseases including many cancers, there remain multiple unknowns concerning how such new materials might overcome the key barriers to drug delivery, namely, the ability to concentrate a therapeutic agent in a target site in sufficient dose and for sufficient time to afford an efficacious response. The potential advantages of polymer pro-drugs are that they can be

Dr. V. Taresco, Dr. T. F. Abelha, Dr. R. J. Cavanagh, C. E. Vasey, Dr. A. B. Anane-Adjei, Dr. A. K. Pearce, Dr. P. F. Monteiro, Prof. K. A. Spriggs, Prof. C. Alexander  
School of Pharmacy  
University Park University of Nottingham  
Nottingham NG7 2RD, UK  
E-mail: cameron.alexander@nottingham.ac.uk

Dr. A. K. Pearce  
School of Chemistry  
University of Birmingham  
Birmingham B15 2TT, UK  
Dr. P. Clarke, A. Ritchie, Prof. S. Martin, Dr. R. Rahman,  
Prof. A. M. Grabowska  
AstraZeneca  
Pharmaceutical Sciences  
Innovative Medicines  
Silk Court Business Park, Macclesfield, Cheshire SK10 2NA, UK  
Dr. M. B. Ashford  
Division of Cancer and Stem Cells  
Faculty of Medicine & Health Sciences  
University of Nottingham  
Nottingham NG7 2RD, UK

 The ORCID identification number(s) for the author(s) of this article can be found under <https://doi.org/10.1002/adtp.202000103>

© 2020 The Authors. Published by Wiley-VCH GmbH. This is an open access article under the terms of the Creative Commons Attribution License, which permits use, distribution and reproduction in any medium, provided the original work is properly cited.

DOI: 10.1002/adtp.202000103

designed to release drugs either at a controlled rate in plasma to ensure drug concentrations remain in the therapeutic window, or they can be encoded with functionality to ensure that release only occurs in the disease site.<sup>[5]</sup> While there have been successes with both approaches,<sup>[6]</sup> there are still significant potential drawbacks.<sup>[7]</sup> For example, in the case of sustained drug release formulations, high concentrations of long-circulating polymer pro-drugs may be needed to maintain the plasma concentration of the drug in the therapeutic range. In delivery systems designed for site-specific release, the concentration of pro-drugs that reach, for example, tumors, is well-documented as being low,<sup>[8]</sup> even though this dose may still be much higher than that achieved by many conventional systemically administered drugs.

In order to address both the above questions, we, and others, have synthesized polymers which enable sustained release in the bloodstream,<sup>[9]</sup> and also which can incur site-specific or externally triggered in situ response.<sup>[10]</sup> We have also been interested in exploring how polymer conformation and architecture alter these and other factors important in delivery, that is, transport in the body, and in crossing tissue, cellular and intracellular barriers. In particular, we are focusing on how polymer and nanoparticle architecture affect the accessibility of linker functionality to biological reagents or conditions,<sup>[11]</sup> and hence how drug release and in vivo efficacy might be controlled both for the “sustained release” types of carriers, and for the “site-specific release” delivery systems. Here we report the evaluation of polymer pro-drugs with the same fundamental chemistries but with three variants of block structures and architectures, and with functionality to attach the well-established anti-cancer drug doxorubicin to the polymer backbone by a serum-stable urea linker. The polymers were based on the poly(ethylene glycol)-*co*-poly(lactide) class of co-polymer micelles, which have entered human clinical use<sup>[12]</sup> but with the hydrophobic block consisting of poly(lactide)-*co*-poly(2-((*tert*-butoxycarbonyl)amino)-3-propyl carbonate), forming polymers we abbreviate as PEG-pLA-pTBPC. Both poly(lactide) and poly(carbonate) polymers are known to be biodegradable, albeit over different time periods, and the presence of the protected side-chain amine in the poly(carbonate) regions allowed us access to further functionality, including drug conjugation, via post-polymerization modification reactions.<sup>[13]</sup> We have studied the behavior of these polymers to assemble into nanoparticles suitable for systemic injection, and have investigated their cytotoxicity in 2D and 3D cell cultures and in vivo. Our specific emphasis for these studies was triple negative breast cancer (TNBC), as this disease is currently addressed poorly with current therapies.<sup>[14]</sup> A number of innovative TNBC formulations and nanosystems have recently been developed, often with multimodal functionality.<sup>[15]</sup> In our case, we suggest that TNBCs in particular might be targeted effectively with highly toxic payloads which are released only in the tumor regions owing to increased activity of proteolytic enzymes, such as plasmin, which have been shown to act also on urea-type pro-drugs in breast cancer.<sup>[16]</sup> We demonstrate that the polymer-doxorubicin pro-drugs are retained in the body of healthy mice for a prolonged period, and show efficacy in reducing the growth of aggressive TNBCs in an orthotopic mouse model. The data also indicate the critical importance of dosing schedules for clinical trial consideration when evaluating the therapeutic activity for amphiphilic polymers with pro-drug functionality.

## 2. Results and Discussion

### 2.1. Polymer Pro-Drug Design, Synthesis, and Characterization in 2D Cell Culture

In this study we designed polymers around three guiding principles; 1) ease of synthesis, 2) similarity to materials in existing clinical practice, and 3) accessible functionality to conjugate a wide variety of therapeutic agents. We considered also some secondary criteria, that is, that the chemistries should be sufficiently flexible so that a single polymer backbone might serve in future as a platform for multiple and/or combinations of drugs, and that the construction might also encode for self-assembly into nanoparticles suitable for systemic injection. Accordingly, we synthesized the polymers by using poly(ethylene glycol), with either methoxy and hydroxyl, or bis(hydroxyl), termini to ring open lactide, and a protected amino-functional cyclic carbonate derived from serinol, to provide a subsequent site for drug conjugation. In this way, we produced materials with poly(ethylene glycol)-block poly(lactide) segments very similar to those of the clinically-used Genexol formulation,<sup>[12]</sup> but with a third component of a degradable polycarbonate with amine-functionality accessible following deprotection. The structures of the initial three candidate polymers P1, P2, and P3 are shown in **Figure 1A**, and the syntheses and primary characterization data (IR, NMR, GPC) were as reported by us recently.<sup>[13]</sup> The polymers differed in terms of the PEG chains used, with a methoxy-PEG<sub>2000</sub> used to initiate lactide polymerization in P1, methoxy-PEG<sub>5000</sub> in P2, and PEG<sub>4000</sub> with two terminal hydroxyl termini used in P3. The effects of these varying PEG components were to modify the self-assembly properties, with changes in micellar-like nanoparticle structure as the polymers ranged from AB-type blocks (P1, P2) to BAB blocks (P3). Dropwise addition of these polymers from acetone solution into excess deionized water resulted in the rapid formation of nanoparticles, which were well-dispersed and colloidally stable in aqueous suspension owing to their negative zeta potential and surface PEG layers (**Figure 1B**). Preliminary characterization of their abilities to enter cells of interest in breast cancers (MCF7, HCC 70, MDA-MB-468, and MDA-MB-231 cells) indicated internalization of Cy5-labelled polymers P1–P3 within 4 h in all cases (**Figure 1C–F**). In addition, the polymers were found to be well-tolerated in the cell lines tested, based on metabolic activity and membrane integrity assays (**Figure S1**, Supporting Information)

Subsequent experiments measured the rate and extent of internalization in selected breast cancer and also healthy breast cells. We also evaluated uptake in THP1 macrophages, as a surrogate measure to indicate likelihood of nanoparticle clearance from circulation, as this is known to occur via macrophage involvement.<sup>[17]</sup> In most cases, the P2 formulation, with the methoxyPEG<sub>5000</sub> hydrophilic outer block and the smallest size (<80 nm) was endocytosed most rapidly and to the greatest extent in the cancer cells (**Figure 2**). The size of nanoparticles played a relevant role on the nanoparticle internalization, as P1 (>100 nm) presented the lowest uptake in the different cell lines. We also observed some cell line specificity in nanoparticle internalization, as P2 and P3 entered MCF7, HCC70, MDA-MB-231, and MDA-MB-468 cells at different rates, but were internalized at similar rates into THP1 derived macrophages. This

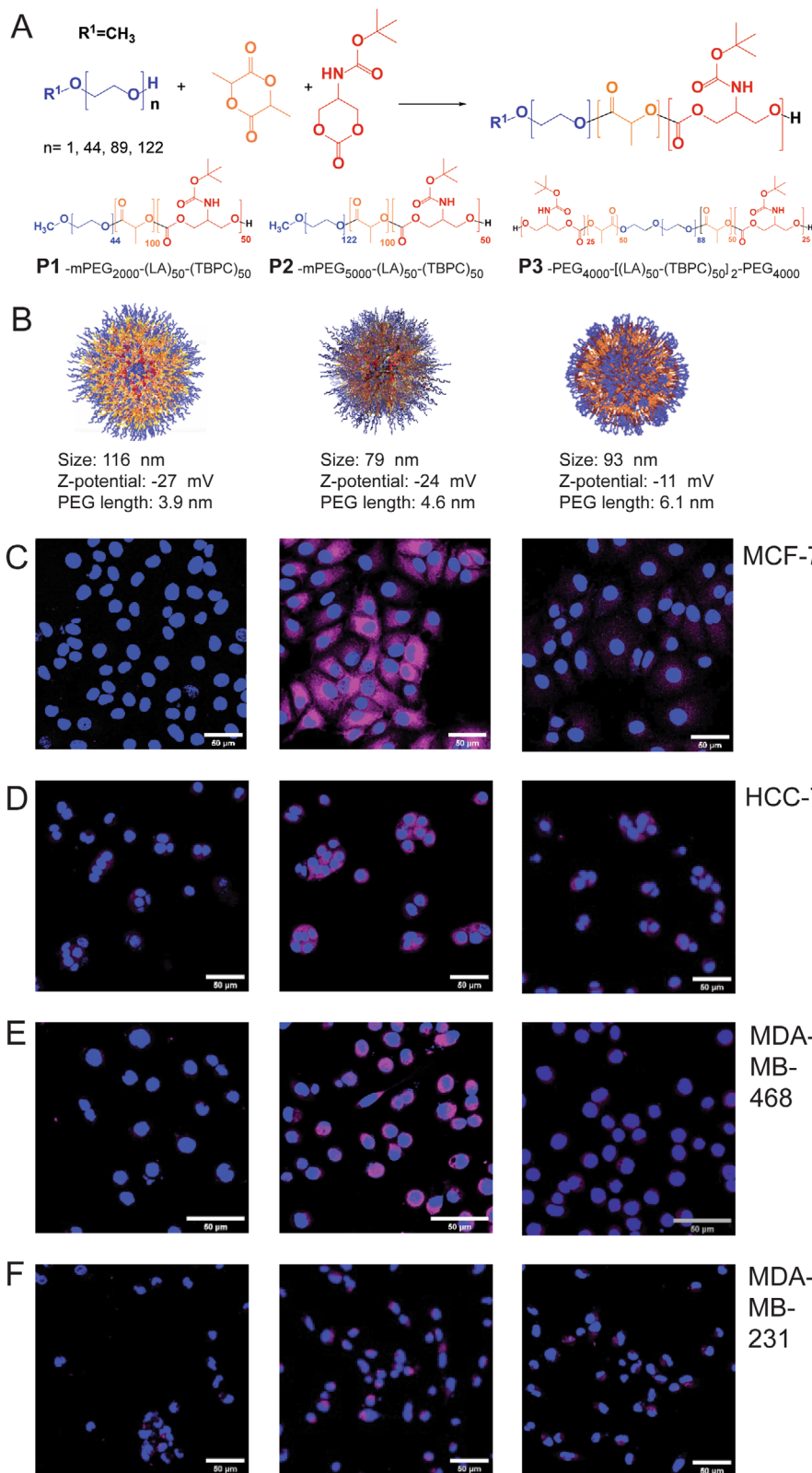


**Figure 1.** In (A) is shown the synthetic route to candidate polymers, with the properties of nanoparticles P1–P3 formed outlined in (B). Plates C–F are confocal micrographs indicating the relevant extent of internalization of P1 (left), P2 (middle), and P3 (right) in MCF7, HCC 70, MDA-MB-468, and MDA-MB-231 breast cancer cells. Uptake of nanoparticles labelled with Cy5 at  $50 \mu\text{g mL}^{-1}$  for 4h. Cy5 and Hoechst nuclei stain fluorescence shown in magenta and blue, respectively. Bar represents  $50 \mu\text{M}$ .

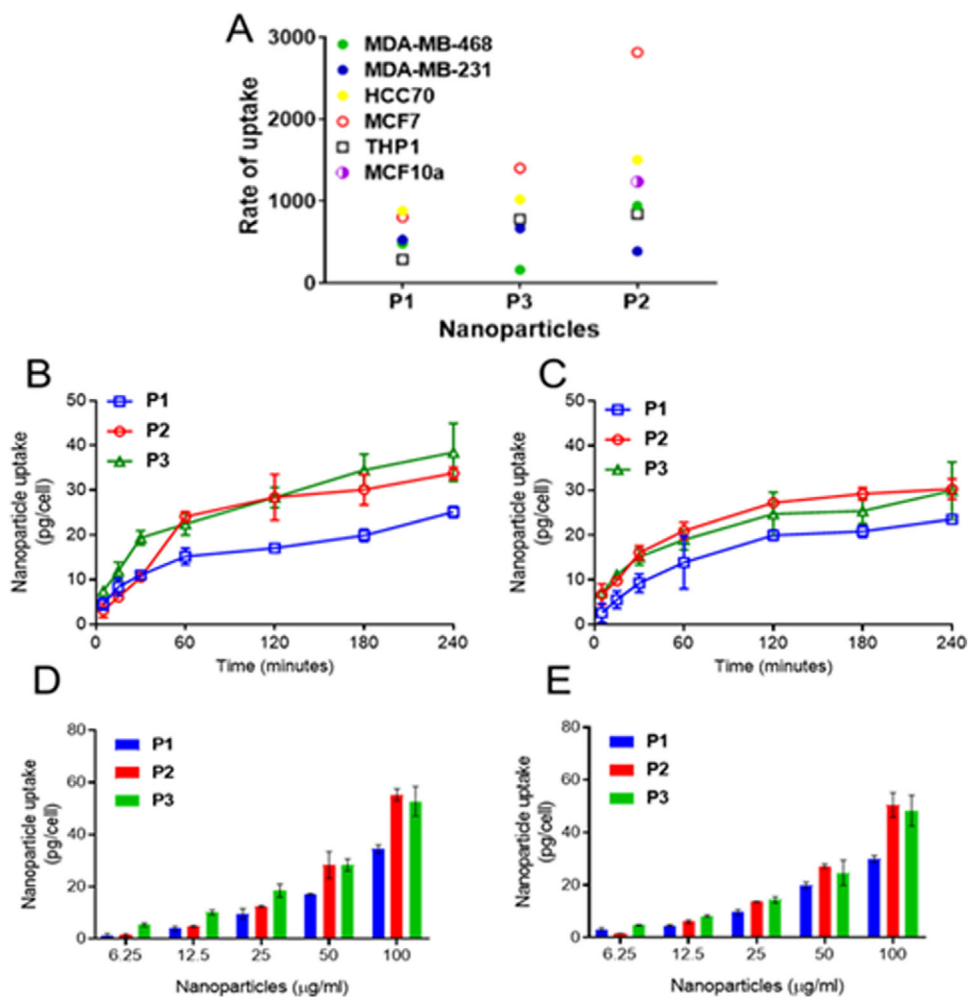


**Figure 2.** A) Rate of uptake of polymer nanoparticles P1–P3 in selected normal breast (MCF-10a), macrophage (THP1), and breast cancer cells (MCF7, HCC 70, MDA-MB-468, and MDA-MB-231). B) Further analysis of the internalization kinetics of P1–P3 ( $50 \mu\text{g mL}^{-1}$ ) in MCF7 cells, and C) MDA-MB-231 TNBC cells revealed an initial high rate of uptake (up to 1 h) followed by a slower period and near steady state at 4 h. D, E) The extent of nanoparticle internalization (at 2 h) was concentration dependent in both D) MCF7 cells and E) MDA-MB-231 TNBC cells.

may have reflected the likely different PEG densities at the surfaces.<sup>[18]</sup>

The mechanisms by which the polymers entered cells were investigated by fluorescence microscopy, in assays wherein nanoparticles were incubated with target cells (MCF7 breast cancer and MDA-MB-231 TNBC) at different temperatures and in the presence or absence of specific (intra)cellular trafficking inhibitors (Figure 3). In these experiments, concentrations were carefully chosen to ensure that all inhibitors were used at concentrations well below toxicity thresholds (Figure S2, Supporting Information, ESI), as prior reports have shown marked effects of certain inhibitors on both metabolic activity and viability of several cancer cell lines.<sup>[19]</sup>

These data indicated that polymer nanoparticle internalization was energy-dependent in both the MCF7 breast cancer cell line and in MDA-MB-231 TNBC cells, as evidenced by the significantly reduced uptake at  $4^\circ\text{C}$  compared to  $37^\circ\text{C}$  (Figure 3B,C). Furthermore, co-localization studies demonstrated that there was some lysosomal accumulation following internal-

ization (Figure 3A). Taken together these data indicate receptor-mediated endocytosis and subsequent trafficking to lysosomes as a potential uptake pathway. It should be noted that the internalization routes were not expected to be mediated by specific receptors, as the polymers were not decorated with any ligands to engage cell surface receptors, however, chlorpromazine significantly reduced uptake of P1–P3 compared to cells not treated with the inhibitor (Figure 3D). These results showed that clathrin-mediated pathways were involved in the internalization of the polymers. Furthermore, genistein significantly reduced the internalization of P2 and P3, indicating that these nanoparticles also exploit caveolin-mediated routes of endocytosis (Figure 3E). Interestingly, P1 internalization was not affected by genistein, suggesting that these larger particles ( $115.8 \pm 7.5 \text{ nm}$ ) are not uptaken via the caveolin-mediated routes. This finding may explain the reduced levels of cellular internalization of P1 compared to P2 and P3 that were observed (Figure 2). Inhibition of dynamine with dynasore resulted in significantly reducing uptake levels of all particles (Figure 3F), supporting the involvement of

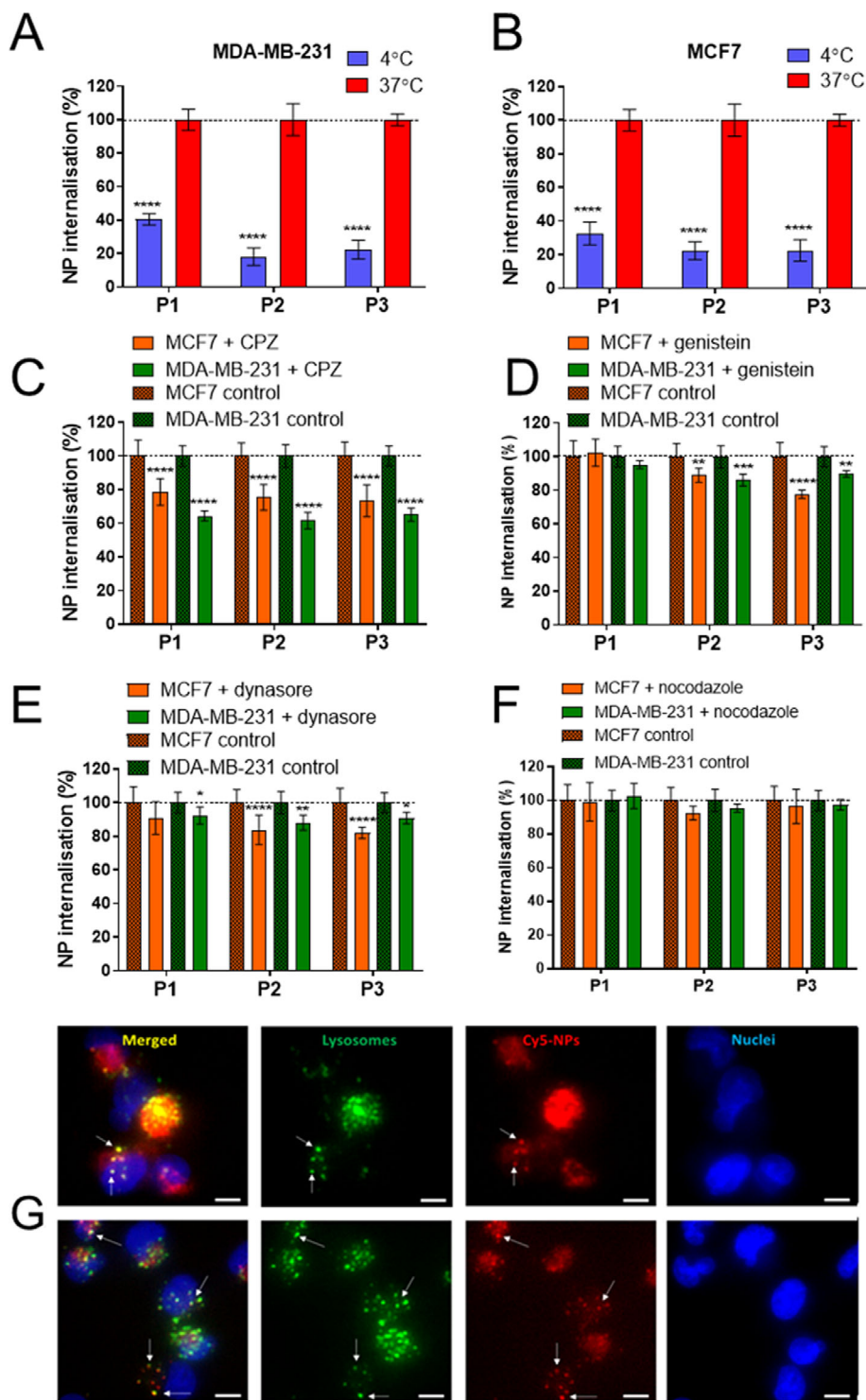


**Figure 3.** Internalization of polymers in selected cell lines. The influence of temperature on P1-P3 nanoparticle uptake in A) MDA-MB-231 and B) MCF7 cells, and C–F) the effect of endocytotic inhibitors on internalization; C) chlorpromazine (CPZ), D) genistein, E) dynasore, and F) nocodazole. Data represent mean  $\pm$  SD ( $n = 3$ ). The group in the presence of NPs but without inhibitor treatment was used as the control groups, and their uptake was expressed as 100%. Statistical significance was determined between control and treated groups by one-way ANOVA followed by Sidak's post hoc test for multiple comparisons (\* $p < 0.05$ ; \*\* $p < 0.01$ ; \*\*\* $p < 0.001$ ; \*\*\*\* $p < 0.0001$ ). Live cell fluorescence microscopy G) of Cy5-labelled P2 nanoparticles co-localization with lysosomes in MDA-MB-231 TNBC cells. Cells were exposed to nanoparticles for 60 min. Cell lysosomes (green) are stained with LysoTracker Green and nuclei with Hoechst 33 342 (blue). Cy5 signal has been colored red to aid visualization of co-localization with green lysosomal signal. The co-localization is indicated in merged panels (yellow) and with white arrows. Two independent repeats are shown from a total of four repeats conducted. Scale bar is 25  $\mu$ m.

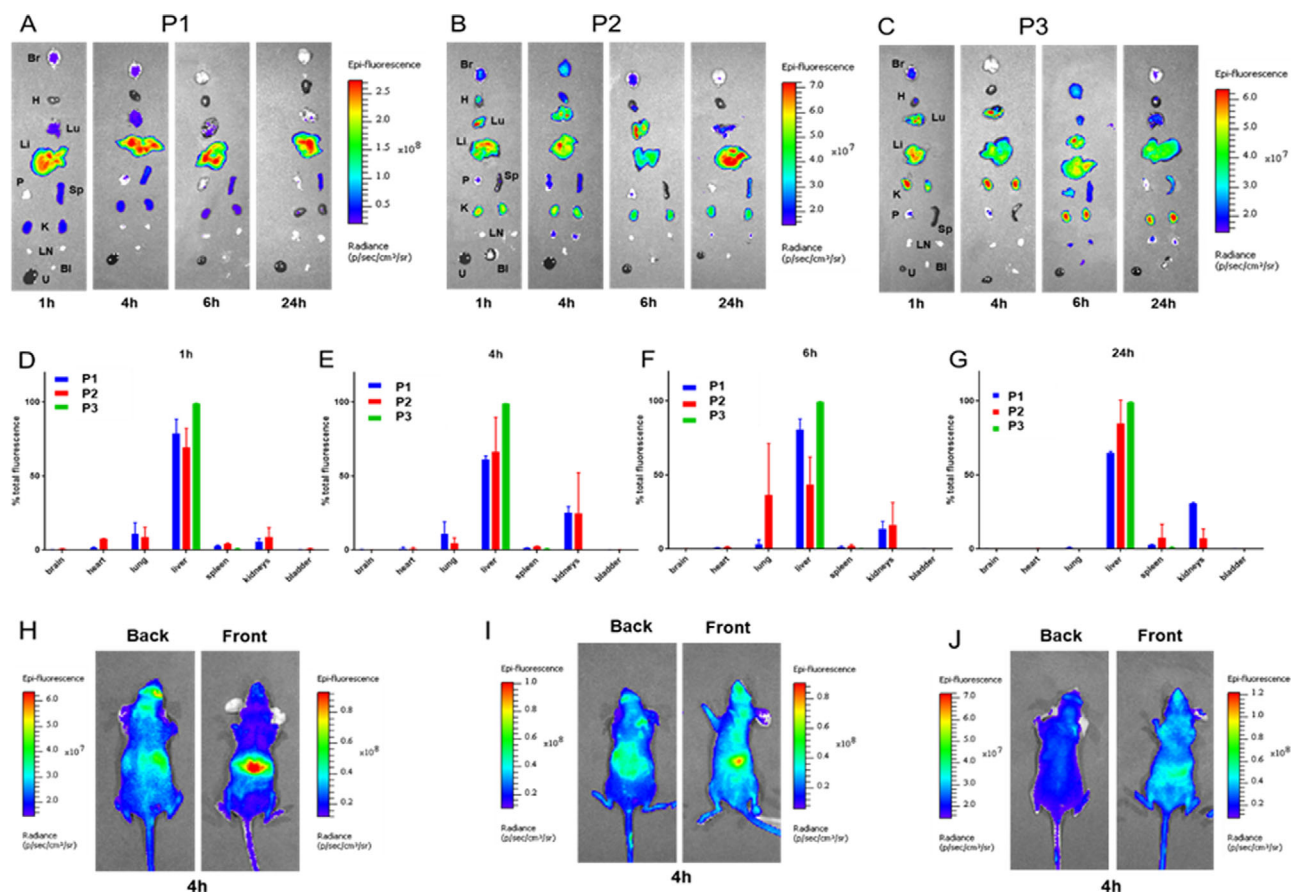


**Figure 4.** Representative ex vivo images at A–C) 1, 4, 6, and 24 h post-injection and quantitation of ex vivo organ data at D) 1h, E) 4h, F) 6h, and G) 24 h, to allow comparison between Cy5-labelled NPs, highlighting the fluorescence signal in organs important for nanoparticle clearance from the bloodstream as a percentage of the total fluorescence in all organs ( $n = 2$ ) (Br: brain, H: heart, Lu: lungs, Li: liver, P: pancreas, Sp: spleen, K: kidneys, LN: lymph nodes, U: urine, Bl: bladder) of A) P1, B) P2, and C) P3. In (H–J) are shown in vivo images of mice treated with Cy5-labelled H) P1, I) P2, and J) P3.

the dynamin-dependent caveolin- and/or clathrin-mediated pathways. Finally, inhibition of microtubule transport with nocodazole demonstrated no significant effect on P1–P3 internalization. In no cases was complete inhibition of internalization demonstrated, showing that uptake likely took place by multiple and simultaneous routes, again in accord with prior assays of non-targeted nanoparticles.<sup>[19,20]</sup>

## 2.2. Tolerability and Biodistribution Studies

We next moved to preliminary experiments to evaluate the primary tolerability and biodistribution of the polymers in healthy mice. Hemocompatibility assays with human blood showed that P2 and its Cy5 variant were not hemolytic below  $30 \mu\text{g mL}^{-1}$  and slightly hemolytic at  $300 \mu\text{g mL}^{-1}$ , (Figure S3, Supporting Information, ES1). The three Cy5-labelled formulations were then injected via tail vein and the organs were imaged after specific time points (Figure 4).

As apparent from the images of the mice during the assays and also of ex vivo isolated organs, the polymers all accumulated in the liver, with P3 showing the highest levels of hepatic uptake at

all time-points. No adverse effects were noted in the mice over the time periods in the assays, indicating that the formulations were well tolerated at the concentrations used ( $500 \mu\text{g mL}^{-1}$ ). When considered in conjunction with the cell internalization data, in which the P2 formulation was the most rapidly internalized, and to the greatest extent, of all the polymers, we decided to focus further on this polymer. In addition, the prior data had shown that P2 nanoparticles were processed to lysosomal compartments and thus might be subjected to degradative pathways which would result in intracellular drug release.

## 2.3. Evaluation of Polymer-Doxorubicin Pro-Drug Penetration and Efficacy in 2D and 3D Cultures

We therefore modified the P2 formulation to carry the well-established cytotoxic drug, doxorubicin, with the chemistries designed such that doxorubicin was conjugated to the polymer backbone via a urea linkage. This linker was chosen in order that the drug should be retained on the polymer during transit in the body, and be more resistant to metabolism in the liver, while being susceptible to proteolytic enzymes overexpressed in

breast cancers which were previously shown to release urea prodrugs.<sup>[16]</sup> Previous studies<sup>[21]</sup> had shown that the doxorubicin urea linker to the polycarbonate backbone was stable at pH 7.4, but that the drug released over time at acidic pH 5.0, and thus we considered the chemistries to be suitable in the first instance for our investigation. NMR analysis indicated that the polymer prodrug, denoted as P4, contained  $\approx 10$  molecules of doxorubicin per chain indicating a coupling yield of  $\approx 80\%$  based on the 12–13 free  $\text{NH}_2$  units available per chain following BOC deprotection. The final weight percentage of doxorubicin in the polymeric prodrug system varied by less than 10% when measured by two spectroscopic techniques (e.g., for 10 units 18% w/w by NMR and 12% by UV–vis). When formed into nanoparticles P4 was slightly larger (130 nm) than its precursor P2 ( $\approx 80\text{nm}$ ), and thus in the first instance, imaging flow cytometry was used to evaluate the internalization of P4 compared to P2 as analogues with different size but the same outer chemical functionality. In addition, it was of interest to characterize further the cellular uptake of P2-Cy5 nanoparticles in relevant breast cancer cells, as we observed that the rate of cell uptake was dependent on the cell type (Figure 2A). MCF7 and MDA-MB-231 presented similar extents of nanoparticle internalization, with the majority of cells showing higher Cy5 fluorescence in their interior compared to the fluorescence within the cell membrane area (Figure 5A,B). As corroborated by our previous finding (Figure 2A), MCF7 presented higher nanoparticle uptake than MDA-MB-231 (Figure 5G), but the former had lower nuclei colocalization than the latter within 4 h incubation time (Figure 5H). When comparing the intracellular distribution of doxorubicin following MDA-MB-231 exposure to P4 nanoparticles and free drug for 48 h, the free drug was found to have reached the nuclei of the entire cell population, whereas  $<31\%$  of cells treated with polymer nanoparticles showed evidence of doxorubicin in cell nuclei as apparent from fluorescence colocalization (Figure 5O).

The P4 polymer-doxorubicin pro-drug was then imaged in more detail in MDA-MB-231 cells by confocal microscopy and tested for efficacy in both 2D and 3D cell culture settings. For these assays, doxorubicin and P4 were dosed at 1  $\mu\text{M}$  equivalent doxorubicin concentration.

The cell-based assays indicated that in 2D culture (Figure 6 and Figure S4, Supporting Information), free doxorubicin was visible in the nuclei of MDA-MB-231 cells within 4 h, while the P4 pro-drug showed preferential accumulation in the cytoplasm (Figure 6A,C and in accordance with Figure 5I–O). However, in the 3D cultures, fluorescence from doxorubicin was apparent throughout the spheroids when P4 was administered, whereas for free doxorubicin, the fluorescent signals were concentrated in the outer layers only (Figure 6B,D). These data demonstrated that P4 either penetrated throughout the  $\approx 500\ \mu\text{m}$  depth of the spheroids as an intact polymer pro-drug, perhaps by multiple transcytosis pathways, and/or that gradual release of doxorubicin took place as the polymer formulation trafficked through the 3D mass. In contrast, the localization of doxorubicin in the spheroid periphery when added as a free drug, was indicative that passive transport of the drug through the 3D structure was slow and less efficient than that of the P4 polymer formulation.<sup>[22]</sup> Extensive washing of the spheroids before and after incubation with the polymers and free doxorubicin was carried out to ensure that any loosely-associated cells were re-

moved, and thus to discount any confounding data from formulations transporting into partly disaggregated cell layers or disrupted spheroids. Comparison of  $\text{IC}_{50}$  values in the MDA-MB-231 cells in 2D culture suggested little difference in potency between the polymer pro-drug and doxorubicin (Figure 6E) but, intriguingly, there were differences in the volumes of the 3D spheroids between free drug and P4 at higher concentrations tested (Figure 6F). At the highest concentration (10  $\mu\text{M}$ ), there was an observed reduction in the spheroid volume of  $\approx 41\%$  and  $56\%$  (Figure S5, Supporting Information) for free doxorubicin and P4 respectively compared with pre-treatment volumes. In addition, it was notable that at some lower concentrations (1 and 0.1  $\mu\text{M}$ ) of doxorubicin equivalent, the P4 formulation was markedly more effective in reducing spheroid volume than doxorubicin alone, which again may reflect different penetration of drug and polymer into the 3D spheroids. For example, the disruption of internal regions by P4 may have led to a greater loss in spheroid integrity, and hence volume, compared to damage to the outermost layers by the free drug. However, it should be noted that spheroid volume is an indirect measure of cytotoxic efficacy in these assays, especially as the spheroids were cultured as tightly-associated cell aggregates, and thus it was perhaps not too surprising that polymer and free drug had similar effects on the spheroid volume at this time point.

#### 2.4. Efficacy Studies of Polymer Doxorubicin Pro-Drug in an Orthotopic Triple Negative Breast Cancer Mouse Model

Since in our case the main interest in these experiments was whether the P4 formulation could penetrate beyond a cell monolayer, we accordingly moved to *in vivo* assays, in which efficacy was evaluated in an orthotopic mouse model of MDA-MB-231 TNBC. It is well-established that such models are complex to establish and the tumors are difficult to treat,<sup>[23]</sup> thus while cognizant of the obvious differences in mouse tumors and human TNBC, we considered this model as an appropriate pre-clinical assay for the P4 formulation.

Tumors were formed in mice following injection of bioluminescent MDA-MB-231 fluc cells into mammary fatpads, with a subsequent growth period of 21 days. Established tumors were confirmed by palpation, and mice were dosed according to two different schedules to take into account the expected longer circulation time of the P4 carrier compared to doxorubicin. The mice were dosed either 3 times in the first week, and then once per week for the next 2 weeks, at doxorubicin (or equivalent) concentrations of 2  $\text{mg kg}^{-1}$ , or 3 times per week for 2 weeks at a doxorubicin concentration (as free drug or as dosed equivalent) of 4  $\text{mg kg}^{-1}$ . In all cases, saline was used as the vehicle control. The experimental schedule included observation of the mice for a further 2 weeks following the treatment period, and monitoring of the health of each mouse via measurements of body mass throughout the assays. The location of Cy5-labelled P4 formulations in the mice following injection was determined by IVIS imaging, and the bioluminescence of the MDA-MB-231 fluc cells was used as a measure of tumor size, with reduced luminescence taken as an indicator of tumor regression. The data from the *in vivo* assays are shown in Figure 7.



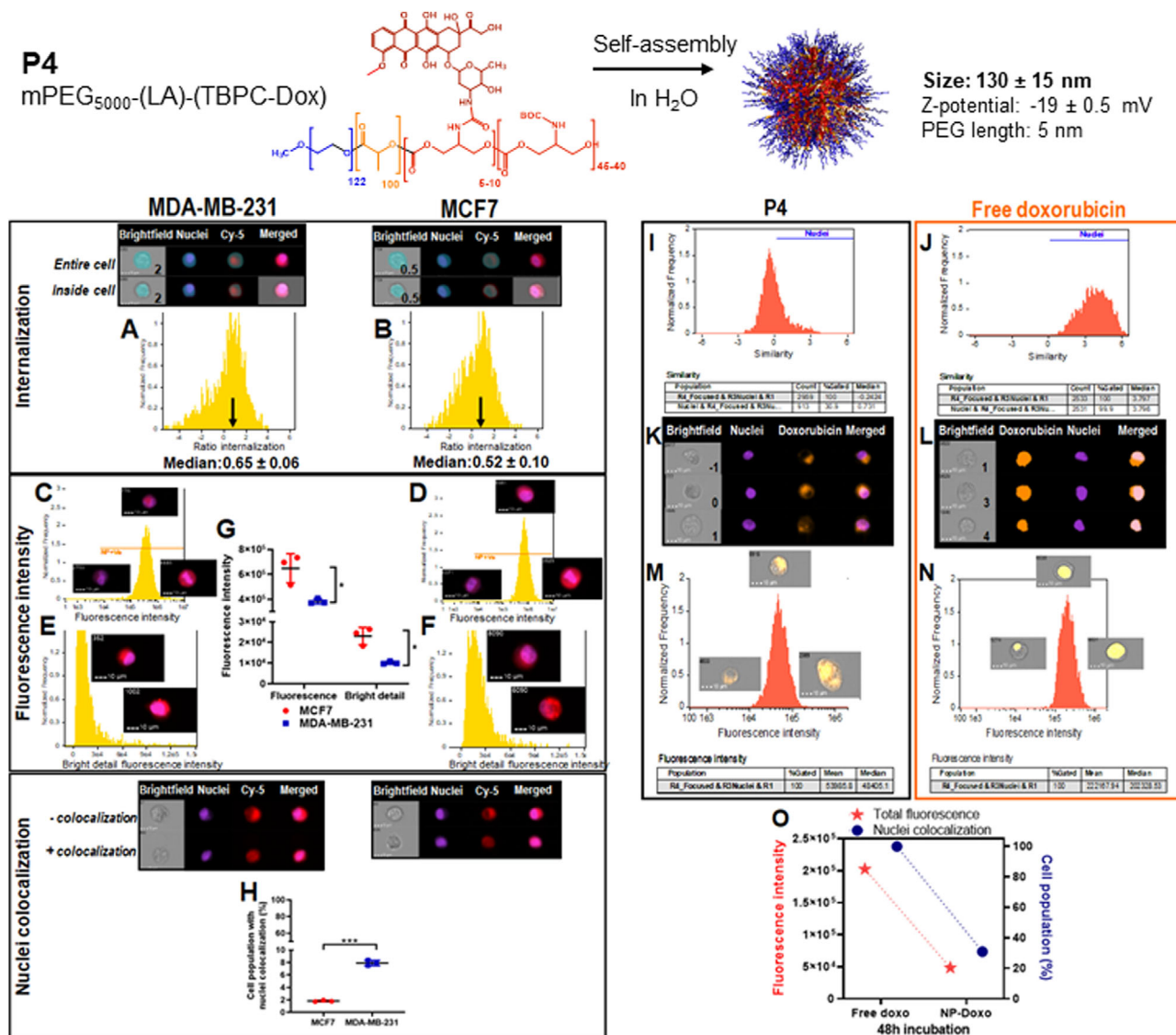


**Figure 5.** Synthesis of P4 (top) and characterization of cellular trafficking of A–H) P2-Cy5 and I–O) P4 via imaging flow cytometry. Left images show the cell masks used to determine the ratio of nanoparticle internalization in A) MDA-MB-231 and B) MCF7 cells. Histograms of Cy5 fluorescence intensity with cell images of correspondent intensities in C) MDA-MB-231 and D) MCF7. Histograms of bright detail fluorescence intensity with top images representing the majority of cells with homogenous uptake and bottom image illustrating cells with nanoparticle accumulation in larger vesicles in E) MDA-MB-231 and F) MCF7. Fluorescence intensity and bright detail fluorescence intensity values of G) MDA-MB-231 and MCF7. H) Nanoparticle nuclei colocalization in both MCF7 and MDA-MB-231. P2-Cy5 nanoparticles were incubated with MDA-MB-231 and MCF7 at 50  $\mu\text{g mL}^{-1}$  for 4 h ( $n = 3$ ). Images on the right show histograms of the ratio of nuclei colocalization of I) P4 and J) the free drug in MDA-MB-231 cells. Pictures illustrating different ratios of nuclei colocalization of K) the nanoparticle and L) the free drug. Histograms of doxorubicin fluorescence intensity of cells exposed to M) the nanoparticle and to N) the free drug. O) Comparison of doxorubicin fluorescence intensity and nuclear colocalization between MDA-MB-231 cells exposed to P4 and free drug. MDA-MB-231 cells were incubated with 1  $\mu\text{M}$  doxorubicin (23  $\mu\text{g mL}^{-1}$  nanoparticles) for 48 h. Data was acquired in a ImageStream Flow Cytometer and analyzed using IDEAS software (v. 6.2, Amnis).

The initial imaging results (Figure 7A) provided evidence that the polymer pro-drug P4 was retained in the bodies of the tumor-bearing mice for prolonged periods, as fluorescence from the Cy5 label on the polymer was visible 24 h after injection (Figure 7A). Since the heart is an organ of concern in cancer therapies due to the dose-limiting cardiotoxicity of free doxorubicin, we measured the fluorescence of excized heart as well as tumors and spleens. Images of these organs (Figure 7B) exhibited Cy5 fluorescence after 24 h, with enhanced accumulation of the polymer formu-

lation in the tumors and spleens compared to the heart. These data were estimated from the luminescence intensities and indicated that tumor accumulation was 17-fold higher than in the heart (radiance values of  $\approx 9.6 \times 10^8 \text{ p s}^{-1} \text{ cm}^{-2} \text{ sr}^{-1}$  in the tumors compared to  $\approx 5.7 \times 10^7 \text{ p s}^{-1} \text{ cm}^{-2} \text{ sr}^{-1}$ ). For mice treated with 2  $\text{mg kg}^{-1}$  equivalent of doxorubicin using 5 doses over 3 weeks the data indicated some differences between the polymer pro-drug P4 and free doxorubicin at individual time-points. Examination of the bioluminescence from the MDA-MB-231

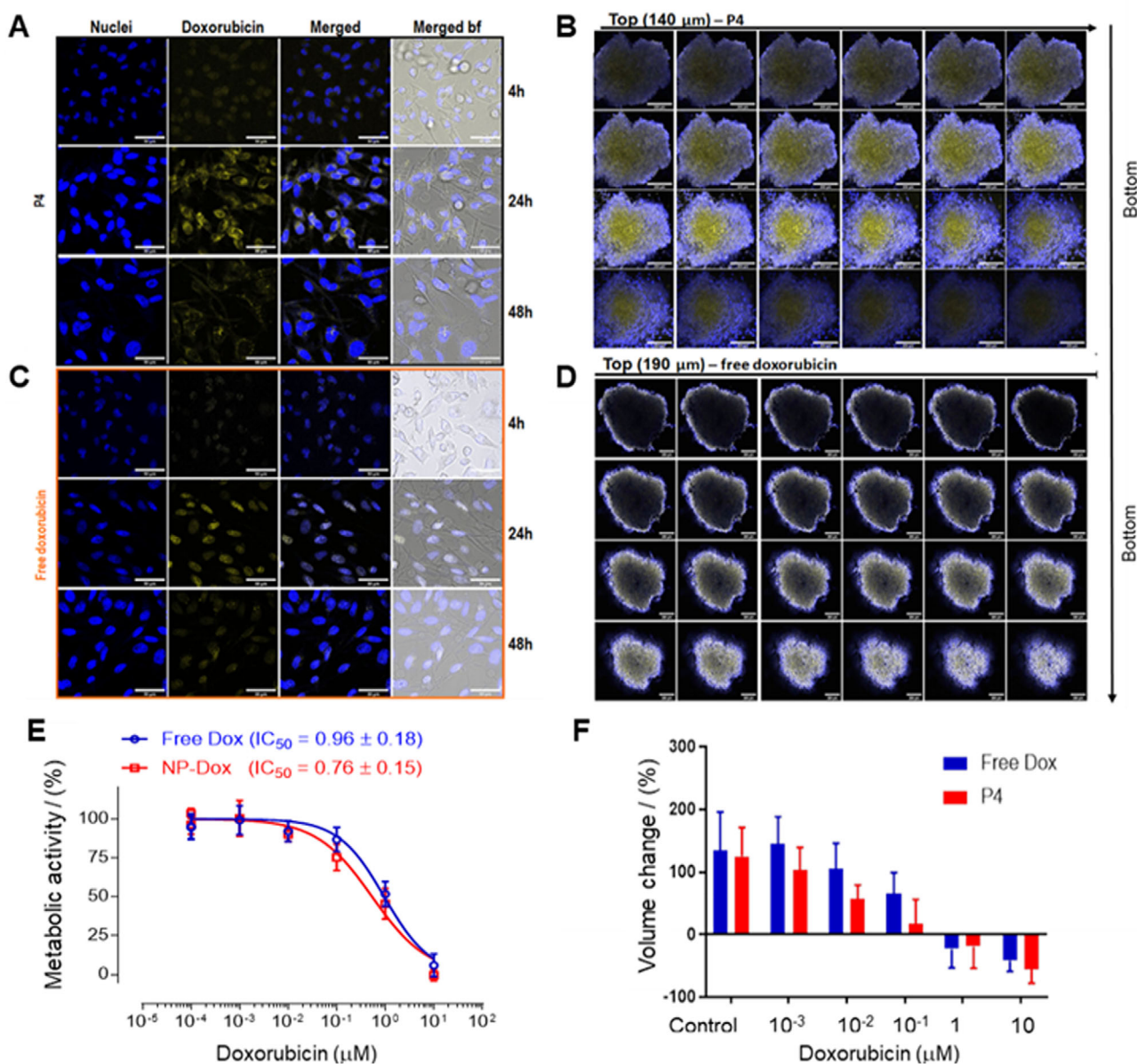


**Figure 6.** Confocal microscopy of MDA-MB-231 cells treated with P4 polymer-doxorubicin pro-drug nanoparticles in A) 2D culture and B) spheroids compared to free doxorubicin in C) 2D and in D) 3D. Cells were exposed to P4 and free drug for 4/24/48 h (2D) and 48 h (3D) at 1  $\mu\text{M}$  doxorubicin ( $23 \mu\text{g mL}^{-1}$  nanoparticles). 3D spheroids images are 5  $\mu\text{m}$  stacks (B/D). Scale bars represent 200  $\mu\text{m}$  (B/D) and 50  $\mu\text{m}$  (A/C). In the micrographs, the Hoechst nuclear stain is depicted in blue, with the fluorescence of doxorubicin false-colored yellow.  $\text{IC}_{50}$  values for P4 compared to doxorubicin in 2D are shown in (E), while (F) indicates volume changes of spheroids following dosing with P4 and doxorubicin respectively.

fluc cells shows that tumors were well-established (Figure 7C–E, left-hand side) at the start of the study, but that there was considerable variation in the sizes of the tumors across the animals. Following treatment (Figure 7C–E, right-hand side), it was apparent that most of the tumors had grown, but there was still considerable heterogeneity in the bioluminescence recorded. Quantification of the data (Figure 7F) indicated that the P4 formulation was slightly more effective than the free drug at the 38 day time-point, but in terms of cumulative efficacy there were no significant differences. However, no serious adverse effects on the mice overall were detected in terms of overall body

weight for the animals which received treatment with the polymer formulations (Figure 7G), and the P4 formulation was better tolerated. These data are thus in accord with prior studies indicating that some delivery systems for doxorubicin improve tolerability of chemotherapy but not overall efficacy.<sup>[24]</sup> For the study in which the mice were treated more frequently, but over a shorter period and at a higher dose ( $4 \text{ mg kg}^{-1}$ ), there was no difference in ability to retard tumor growth for free doxorubicin compared to P4 (Figure S6, Supporting Information), but both treatment groups showed efficacy as expected against vehicle control. In addition, data from H+E staining of tumors

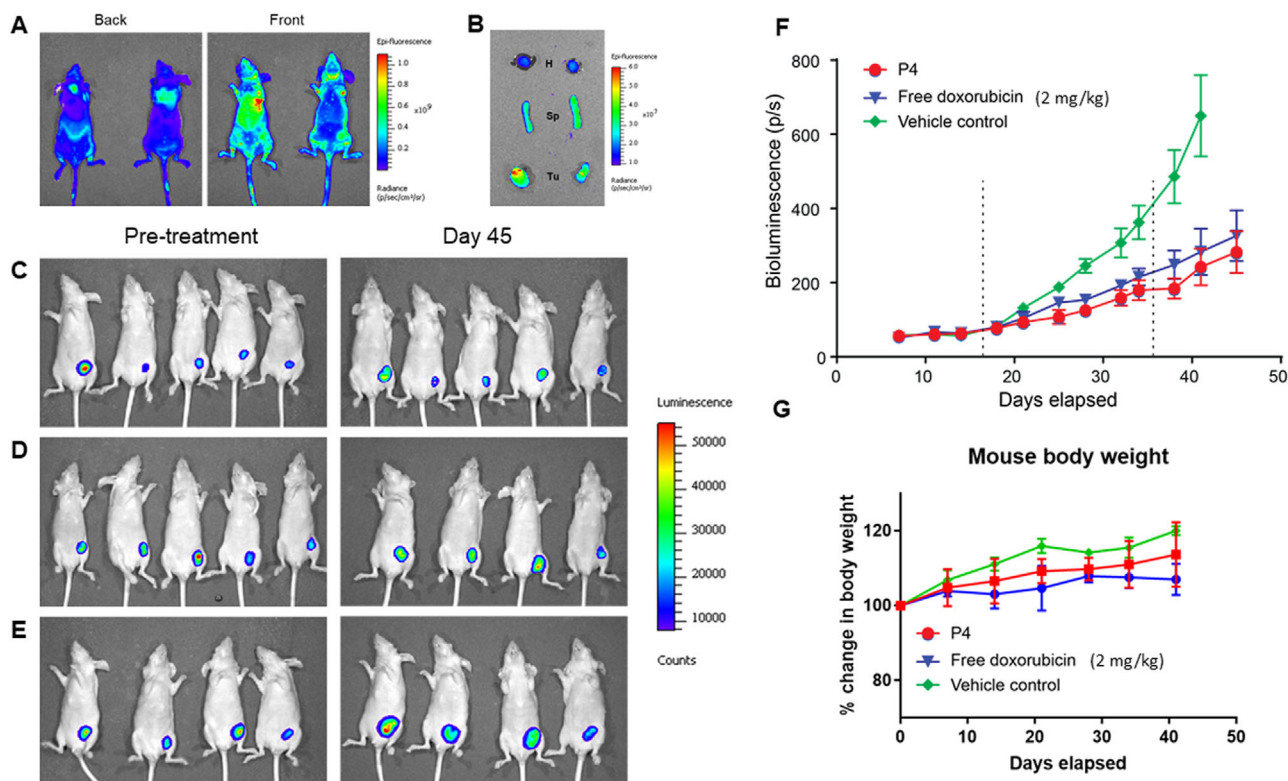


**Figure 7.** Fluorescence images of Cy5-labelled P4 nanoparticles captured 24 h after injection into MDA-MB-231 tumor-bearing mice A) in vivo and B) ex vivo with organs (H: heart, Sp: spleen, T: tumor). In (C–E) are shown luminescence images of MDA-MB-231 fLuc tumor-bearing mice at day 17 (pre-treatment) and prior to termination (day 45) for the treatment groups C), P4, D) free doxorubicin, and E) vehicle control (saline) following dosing with  $2 \text{ mg kg}^{-1}$  equivalent of doxorubicin using 5 doses over 3 weeks. In (F) are shown tumor volumes as measured by bioluminescence intensities of MDA-MB-231 fLuc following dosing with  $2 \text{ mg kg}^{-1}$  equivalent of doxorubicin using 5 doses over 3 weeks. The dotted lines indicate the dosing period. In (G) are shown body weight changes of MDA-MB-231 tumor-bearing mice during treatment (10 animals per group). Free doxorubicin and P4 were dosed with  $2 \text{ mg kg}^{-1}$  equivalent of doxorubicin using 5 doses over 3 weeks as described for data in (C–F). Data expressed as mean  $\pm$  SD.

recovered at the end of the treatment period (Figure S7, Supporting Information) showed no difference between P4 and free drug, suggesting that at the higher and more frequent dosing, there was no advantage to using the polymer formulation. From the histological analysis, the distribution of H+E positive cells was not significantly altered for mice treated with free doxorubicin compared to P4. It might be expected that the nanoparticle formulation might not transport away from the blood vessels as easily as free doxorubicin, but from H+E stains alone it was not possible to determine whether the penetration of free drug and P4 into the tumors was the same, or whether P4 had penetrated further but released doxorubicin less efficiently in the tumors as compared to release in the prior 3D spheroid experiments.

When considered as a whole, the data are revealing, as they indicate marked differences between the performance of the polymer formulation in the 3D spheroids and in vivo. There have been many discussions on the limits of tissue models, and indeed pre-clinical animal models, and their relevance for translation to human clinical performance.<sup>[25]</sup> However, recent papers have indicated some successes in using advanced 3D cancer spheroids for screening cancer drug formulations,<sup>[26]</sup> and our data showed that in the 3D cultures, the P4 formulation transported well through the densely packed cell layers. In addition,

it has been very recently shown that transcytosis is an important pathway for nanoparticle transport in tumors.<sup>[27]</sup> Therefore, it is possible to speculate that the efficacy of the P4 formulation compared to the free drug in the dense compacted spheroids may be partly accounted for by multiple transcytosis events. However, the lack of any significant efficacy difference in vivo between the P4 doxorubicin polymer pro-drug and doxorubicin itself is less easy to attribute to intercellular transport differences. The P4 formulation contained a urea linkage, and thus while cytotoxicity was observed with the polymer pro-drug, the rate or location of release of doxorubicin within the tumor regions may not have been any different to that of the free drug itself. It should be noted that the polymers used in this study were deliberately not “targeted”, as in order to maintain as simple a formulation as possible for potential translation, we did not attach any ligands to the polymers which might have aided internalization in specific regions of the tumor. Thus we were reliant on the inherent passive accumulation of the polymers in the tumors, and without detailed analysis of the individual tumors in the mice, it is not possible to indicate whether vasculature may have been disrupted or any EPR effect might take place in these regions. The EPR phenomenon has been widely discussed in the context of cancer biology in both pre-clinical and human studies,<sup>[28]</sup> but is not a feature of all cancers and is highly tumor-dependent. The

H+E data did not show marked differences between areas of the tumor for mice treated with doxorubicin and the polymer formulation P4. However, without in depth cell and tissue analysis to ascertain at what rate doxorubicin reached the tumors or was released from the polymers in tissue we cannot identify clearly why P4 was more effective in vitro compared to free drug but not in vivo. Our future studies will address in more detail if transcytosis pathways or transport in tumor regions are the more dominant factors in the efficacy of these and related polymers.

### 3. Conclusions

The experiments reported here have shown that a range of amphiphilic polymers, derived in simple steps from accessible precursors and with components similar to those used in clinically-applied formulations, can be assembled into kinetically-trapped micellar-like nanoparticles. These rapidly entered a range of breast cancer cells by energy-dependent routes in 2D cell culture, and were found to be well-tolerated and with no identifiable adverse effects when injected systemically in mice. A side-chain derivatized polymer pro-drug variant, with doxorubicin attached by a urea linker, was shown to be more effective in penetrating through dense-packed spheroids of TNBC MDA-MB-231 cells than free doxorubicin. Although the polymer pro-drug displayed enhanced therapeutic potential in the spheroids, it was not significantly more potent in reducing tumor volume in an aggressive orthotopic MDA-MB-231 tumors in mice. However, no weight loss was observed in the mice following administration of the polymer-doxorubicin conjugate, suggesting that future studies might focus on changes in dosing schedules to maximize therapeutic window, as is applied clinically for current liposomal doxorubicin formulations. We believe these “first generation” materials, which are biodegradable and similar to those used in current human cancer therapies, but which have the advantage of additional functional groups allowing attachment of combination drugs and targeting ligands, might advantageously be developed further for cancer therapies.

### 4. Experimental Section

**Materials:** Standard reagents, solvents monomers and other materials for chemical synthesis were purchased from ThermoFisher or Sigma-Aldrich and used without further purification. HuMEC basal serum free medium (cat. # 12653-018), bovine pituitary extract medium (cat. # 13028-014), HuMEC supplement kit (cat. # 12754-016), and high glucose DMEM (phenol red free, cat. # 31053-028) were acquired from Gibco (Life technologies). High glucose DMEM (cat. # D6546), RPMI-1640 medium (phenol red free cat. # R7509 and with phenol red cat. # R0883), Trypsin-EDTA (cat.# T3924), TOX7 LDH kit (cat. # 1002 455 517), Phorbol 12-myristate 13-acetate (PMA, cat.# P8139), foetal bovine serum (FBS, cat.# F7524), penicillin-streptomycin antibiotic solution (10 000 U penicillin and 10 mg mL<sup>-1</sup> streptomycin, cat. # P0781), L-glutamine (200 mM, cat. # G7513), and DMSO (cat.# D2438) were purchased from Sigma-Aldrich. Hoechst 33 342 (cat.# H1399) and Presto Blue 10x solution (cat. # A13262 100 mL) were acquired from Invitrogen.

**Polymer Synthesis:** Polymers P1–P3 were synthesized as reported previously,<sup>[13]</sup> using methoxy poly(ethylene glycol) (MeO-PEG) of approximate molar masses of 2000 Da and 5000 Da, and a dihydroxyPEG of approximate molar mass of 4000 Da to ring-open lactide and a

BOC-protected cyclic carbonate monomer derived from serinol. Accordingly, a predetermined amount of PEGylated chain initiator (mPEG<sub>2000</sub>, mPEG<sub>5000</sub>, or PEG<sub>4000</sub>), lactide, and the BOC-protected cyclic carbonate were added to a pre-dried glass vial and capped. In order to maintain a constant length of hydrophobic chains for each PEGylated chain initiators, [M]/[I] was adjusted accordingly. Dry dichloromethane (5–10 mL), was added at room temperature, followed by 1,8-diazabicyclo[5.4.0]undec-7-ene (DBU, 2–3% mol/mol compared to the total amount of monomers) which was dissolved in extra dichloromethane (1 mL) and added to catalyze the polymerization. After the reaction was complete, the catalyst was deactivated and the polymers were purified via multiple solvation and precipitation steps from dichloromethane into hexane and dried in vacuum. Typical yields for conversion of monomer to polymer were 75–80% w/w.

**Labelling of Polymers with Cy5:** The same reaction conditions were used for polymers P1–P3 to conjugate an amine-functional Cy5 to the hydroxyl-terminus of the polymers via disuccinimidyl carbonate (DSC) coupling. A sample of polymer (100 mg), triethylamine (TEA, excess; 10 µL) in dry MeCN (0.5 mL) and DSC (excess; 5 mg) in dry MeCN (1 mL) was added to a dry glass vial under continuous stirring at 0 °C and left for 3 h. A stock solution of Cy5-amine and TEA was prepared in dry MeCN, with Cy5 at 1% wt/wt to the polymer and the TEA concentration in excess with respect to the dye. Henceforth, 1 mg Cy5 and 10 µL TEA were dissolved in 2 mL dry MeCN. This was then added to the reaction under constant stirring at 0 °C and left for a further 3 h. Subsequently, the resultant conjugated polymer was purified through multiple precipitation steps in cold hexane:diethyl ether (3:5 v/v) and left to dry in a vacuum oven to yield Cy5-conjugated polymer. The Cy5 content in the mixed micelles was calibrated against Cy5-amine standards ( $\lambda_{exc} = 647$  nm,  $\lambda_{em} = 665$  nm) using fluorescence, based on a published procedure.<sup>[21]</sup>

**BOC Deprotection:** A predetermined amount of PEGylated copolymer was dissolved in extra dry dichloromethane (3 mL). The optimum amount of trifluoroacetic acid was found to be 5 eq with respect to the calculated tBSC units and was added slowly to the polymer mixture at 0 °C. The reaction mixture was left stirring for 20 min, and following precipitation in cold hexane, was washed with cold diethyl ether and analyzed by <sup>1</sup>H NMR after complete drying. <sup>1</sup>H NMR ( $t = 0$  min) (400 MHz, DMSO-d<sub>6</sub>)  $\delta = 5.26$ – $5.10$  (m, 80H),  $4.17$ – $4.01$  (m, 168H),  $3.52$  (s, 492H),  $1.48$  (s, 240H),  $1.39$  (s, 370H). <sup>1</sup>H NMR (after 20 min and post purification and drying) (400 MHz, DMSO-d<sub>6</sub>)  $\delta = 8.42$  (bs, 30H),  $7.18$ – $7.02$  (m, 34H), ( $\approx 10$  units deprotected)  $5.24$ – $5.11$  (m, 62H),  $3.51$  (s, 492H),  $1.55$ – $1.41$  (m, 204H),  $1.38$  (s, 320H).

**Coupling of Doxorubicin to Polymer P2 to Form Polymer P4:** N,N'-disuccinimidyl carbonate (DSC) (1.5 eq. with respect to the amount of doxorubicin, 0.125 mmol, 32 mg) pre-dissolved in anhydrous MeCN (3 mL) was added to a solution of doxorubicin (1.0 eq., 0.083 mmol, 48 mg) in dry DMSO (3 mL) at 0 °C. Triethylamine (2.5 eq. with respect to the amount of doxorubicin, 0.21 mmol, 30 µL) was added slowly to the reaction mixture and left stirring for 4–5 h. Deprotected polymer P2; 1.0 eq., 0.083 mmol, 15 mg; equivalents were calculated to be in excess when compared to each repeating carbonate backbone unit) was dissolved in a mixture of anhydrous MeCN/ dry DMSO (50/50, v/v, 3 mL) and TEA (2.0 eq. with respect to the amount of deprotected polymer, 0.166 mmol, 23 µL) was added, and the solution was subsequently added dropwise to the previous reaction mixture. The reaction was left stirring for a further 3 h at 0 °C. The resultant drug-conjugated polymer was purified through multiple precipitation steps in cold hexane:diethyl ether (1:5 v/v) mixture and dialyzed against water:methanol (5:1 v/v) mixture for 24 h. Finally, the purified aqueous suspension was freeze-dried for 48 h and stored at –22 °C.

<sup>1</sup>H NMR (400 MHz, DMSO-d<sub>6</sub>)  $\delta = 14.08$  (s, 4H),  $7.93$  (d,  $J = 4.3$  Hz, 8H),  $7.69$ – $7.65$  (m, 4H),  $7.63$  (s, 4H),  $7.07$  (d,  $J = 7.1$  Hz, 21H),  $5.34$  (d,  $J = 8.7$  Hz, 8H),  $5.24$ – $5.11$  (m, 78H),  $4.86$  (d,  $J = 5.9$  Hz, 4H),  $4.61$ – $4.56$  (m, 4H),  $4.50$  (d,  $J = 10.1$  Hz, 8H),  $4.36$  (d,  $J = 4.0$  Hz, 12H),  $4.16$ – $3.93$  (m, 205H),  $3.81$ – $3.74$  (m, 8H),  $3.71$ – $3.66$  (m, 4H),  $3.51$  (s, 492H),  $3.24$  (s, 4H),  $3.07$ – $3.01$  (m, 8H),  $2.94$  (d,  $J = 5.9$  Hz, 4H),  $2.23$  (d,  $J = 3.8$  Hz, 4H),  $1.50$ – $1.41$  (m, 200H),  $1.38$  (s, 290H).

**Nanoparticle Preparation and Characterization:** Kinetically-trapped micellar-like polymer nanoparticles were prepared as described

previously.<sup>[13]</sup> For all the polymers, a solvent–non-solvent precipitation method was used to form nanoparticles, in which the polymers (10 mg) were dissolved in acetone (1 mL) and added dropwise to deionized water (10 mL, final concentration of 1 mg mL<sup>-1</sup>). Stirring at 550 rpm was maintained throughout the addition steps to allow stable nanoparticle suspensions to form. The resultant suspensions were stirred overnight at room temperature to ensure no solvent remained. All nanoparticle suspensions were filter-sterilized (0.2 µm membrane) prior to *in vitro* and *in vivo* studies.

**Cell Culture:** All cells were purchased from the American Type Culture Collection (ATCC; Manassas, Virginia). MDA-MB-231, MCF7, MCF-10A, HCC70, and MDA-MB-468 cells were used in a passage window of 15, and RAW 264.7 cells in a passage window of 10. MDA-MB-231, MDA-MB-468, HCC70, and MCF7 cells were cultured in DMEM (Sigma-Aldrich) and RAW 264.7 in RPMI (Sigma-Aldrich). Both media types were supplemented with 10% (v/v) foetal bovine serum (FBS; Sigma-Aldrich) and 2 mM L-glutamine (Sigma-Aldrich). THP1 monocytic cells were cultured in RPMI medium supplemented with 10% FBS, 1% L-glutamine (200 mM), and 1% antibiotic solution (penicillin-streptomycin). THP1 cells were maintained with medium replacement by centrifugation and subcultured prior to cell population reaching 10<sup>6</sup> cells mL<sup>-1</sup>. For differentiation, THP1 cells (312 500 cells cm<sup>-2</sup>) were subcultured in appropriate dishes with antibiotic free medium supplemented with 100 ng mL<sup>-1</sup> (162 nM) PMA for 2 days. MCF10a epithelial breast cell line was grown in HuMEC basal serum free medium supplemented with bovine pituitary extract medium and HuMEC supplement kit. Culture conditions were maintained at 37 °C with 5% CO<sub>2</sub> and 90% relative humidity.

**In Vitro Nanoparticles Internalization Studies in Cancer Cells: Fluorometric-Based Method:** MCF7 and MDA-MB-231 breast cancer cells were plated at 1 × 10<sup>4</sup> cells per well in 96 well plates and RAW 264.7 macrophages seeded in 12 wells plates at a density of 1.2 × 10<sup>5</sup> per well. Following a 24 h culture period, culture medium was removed and Cy5-labelled nanoparticles were applied in phenol red free medium containing 10% (v/v) FBS. The time-dependence of cell uptake was assessed with 50 µg mL<sup>-1</sup> solutions of nanoparticles and at time points of 15, 30, 60, 120, 180, and 240 min. Additionally, the concentration-dependence of uptake was investigated at a fixed time point of 2 h with nanoparticle solution concentrations of 6.25–100 µg mL<sup>-1</sup>. Following exposure, nanoparticle solutions were removed and cells washed three times with ice cold PBS. Cells were then permeabilized with 1% (v/v) Triton X-100 solution applied in PBS for 10 min at 37 °C. Permeabilized cells were thereafter pelleted by centrifugation and nanoparticles quantified by fluorescent measurement at 640/680 nm ( $\lambda_{ex}/\lambda_{em}$ ). Quantification of nanoparticle uptake was achieved via calibration curves of known nanoparticle concentrations diluted in 1% (v/v) Triton X-100 in PBS solution. Values were normalized to viable cell number per well determined by the trypan blue exclusion test and cell counting on a hemocytometer.

**Flow Cytometry Assays for Assessment of Nanoparticle Internalization and Transport:** To characterize the rate of nanoparticle internalization, MCF7, MCF10a, MDA-MB-231, MDA-MB-468, and HCC70 (31 250 cells cm<sup>-2</sup>) and THP1 derived macrophages (312 500 cells cm<sup>-2</sup>) were incubated with 50 µg mL<sup>-1</sup> P1/P2/P3-Cy5 for 15 min, 30 min, 1 h, and 4 h, then the cells were thoroughly washed with PBS, preserved with 4% PFA in PBS, detached using trypsin-EDTA and resuspended in 500 µL PBS. Fluorescence was acquired under 488 nm excitation and 655–685 nm emission bandwidth in a FC500 flow cytometer (Beckman Coulter). The median fluorescence intensity values of homogeneous and healthy cell populations was used to quantify the cell uptake. To quantify nanoparticle internalization rates in the different cell lines, the slope of the curve of regression analysis of fluorescence intensity versus incubation time was normalized by each nanoparticle fluorescence intensity (histograms can be found in Figure S8, Supporting Information). Nanoparticle internalization and nuclei colocalization was performed for P2-Cy5 (50 µg mL<sup>-1</sup>; 4 h incubation) in both MCF7 and MDA-MB-231 cells and P4/free doxorubicin (1 µM doxorubicin; 23 µg mL<sup>-1</sup> nanoparticle; 48 h incubation) in MDA-MB-231 cells at 31250 cells cm<sup>-2</sup>. Following exposure to the different treatments, the cells were incubated with Hoechst 33 342 at 2 µg mL<sup>-1</sup> for 10 min. Then, they were thoroughly washed with PBS, preserved with 4% PFA in PBS, detached us-

ing trypsin-EDTA, and resuspended in 50 µL PBS prior to acquiring the images in an Image Streamx Mk II Imaging Flow Cytometer (Amnis) with 40x magnification. The data analysis was performed using IDEAS Image Stream Analysis Software (Amnis). The imaging flow cytometry analysis of nanoparticle internalization represents ratio of the intensity inside the cell to the intensity of the entire cell and accounts for the preferential accumulation inside the cell compared to that in the cell membrane. The cell uptake is represented by the total fluorescence intensity. The bright detail is the intensity of localized bright spots within the masked area in the image and a high value is related to the nanoparticle distribution into larger vesicle-like structures rather than homogeneously distributed in the cytoplasm.

**Confocal Microscopy Imaging:** Confocal microscopy analysis was carried out in cells sub-cultured in glass dishes (CELLview culture dish, Greiner Bio-One, Germany). MCF7, MDA-MB-231, MDA-MB-468, and HCC70 (31 250 cells cm<sup>-2</sup>) and THP1 derived macrophages (312 500 cells/cm<sup>2</sup>) received P1/P2/P3-Cy5 at 50 µg mL<sup>-1</sup> for 4 h and MDA-MB-231 cells were treated for 4/24/48 h with P4/free doxorubicin (1 µM doxorubicin/23 µg mL<sup>-1</sup> nanoparticle). In sequence, they were incubated with Hoechst 33 342 at 5 µg mL<sup>-1</sup> for 10 min, carefully washed with warm PBS and preserved with 4% paraformaldehyde in sterile PBS. MDA-MB-231 3D spheroids grown for 3 days were treated with P4/free doxorubicin (1 µM doxorubicin/23 µg mL<sup>-1</sup> nanoparticle) for 48 h. Then, they were incubated with Hoechst 33 342 at 5 µg mL<sup>-1</sup> for 10 min and were carefully washed with warm PBS and preserved with 4% PFA in sterile PBS. The visualization of intracellular probe accumulation was performed in a TCS SPE Leica confocal microscope using 40x (2D cells) and 10x (3D spheroids) objectives and the images were analyzed using ImageJ software.

**Live Cell Fluorescence Microscopy:** Cells were seeded in 96 well plates at a density of 1 × 10<sup>4</sup> cells per well. Cells were incubated with 50 µg mL<sup>-1</sup> Cy5-labelled nanoparticle solutions for 60 min. Cells were then stained with Hoechst 33 342 (10 µg mL<sup>-1</sup>) and LysoTracker Green (50 nM) for 30 min and imaged on an inverted Nikon Eclipse TE 300 microscope on DAPI, FITC, and Cy5 filters. Images were merged using ImageJ software.

**Assessment of Internalization Mechanisms:** To study the uptake mechanisms of nanoparticles, chlorpromazine (CPZ; 30 µM), genistein (35 µM), nocodazole (35 µM), and dynasore (20 µM) were applied to inhibit clathrin-mediated, caveolin-mediated, microtubule-mediated, and dynamin-dependent endocytotic routes, respectively. Nanoparticle internalization was assessed via the fluorometric-based method (described above) with the following amendments; cells were pre-incubated with inhibitors for 30 min, followed by application of nanoparticle solutions, spiked with inhibitor, for 240 min.

**Cytotoxicity Experiments:** The PrestoBlue cell viability assay (Thermo Fisher Scientific) and the lactate dehydrogenase (LDH) release assay (Sigma Aldrich, TOX7 kit) were performed to assess nanoparticle cytotoxicity. All cell types, but THP1 (see cell culture section above), were seeded at 1 × 10<sup>4</sup> cells per well in 96 well plates and cultured for 24 h prior to assaying. Nanoparticles were exposed to cells for 48 h and applied in 100 µL phenol red free DMEM containing 10% (v/v) FBS and 2 mM L-glutamine. Triton X-100 applied at 1% (v/v) in phenol red free DMEM was used as a cell death (positive) control and a vehicle control containing no nanoparticles used as a negative control. Following exposure, 50 µL of supernatant was collected per well for analysis of LDH content. Cells were washed twice with warm PBS and 100 µL 10% (v/v) PrestoBlue reagent diluted in phenol red free medium applied per well for 60 min at 37 °C. The resulting fluorescence was measured at 560/600 nm ( $\lambda_{ex}/\lambda_{em}$ ). Relative metabolic activity was calculated by setting values from the negative control as 100% and positive control values as 0% metabolic activity. Assessment of LDH release was performed according to the manufacturer's instructions and involved adding 100 µL LDH detection reagent to the collected supernatant samples and incubating at room temperature shielded from light for 25 min. Absorbance was measured at 492 nm. Relative LDH release was calculated with the negative control absorbance at 492 nm taken as 0%, and the positive control, assumed to cause total cell lysis, as 100%.

**Hemolysis:** The nanoparticle hemolysis assay was performed according to a standard method for nanoparticle hemocompatibility.<sup>[29]</sup> Briefly, fresh human blood was mixed to anticoagulant (1:10, citrate buffer: blood)

and the hemoglobin content in blood was determined. The assay was performed at standard  $10 \text{ mg mL}^{-1}$  hemoglobin concentration. Triton-X-100 ( $10 \text{ mg mL}^{-1}$ , positive control), DPBS (negative control), PBS (vehicle control), and nanoparticles at 3; 30 and  $300 \text{ } \mu\text{g mL}^{-1}$  were incubated for 3 h at  $37 \text{ }^\circ\text{C}$  with gentle mixing every 30 min. The percent hemolysis induced by a test sample can be classified as non-hemolytic if lower than 2%, slightly hemolytic within 2–5% and hemolytic if higher than 5%.<sup>[30]</sup>

**3D Spheroid Assays:** For doxorubicin and P4 confocal microscopy assays, MDA-MB-231 spheroids were prepared by the hanging drop method, in which 5000 cells were cultivated for 3 days prior to receiving the appropriate treatment. In the imaging assays, MDA-MB-231 spheroids were treated after 3 days with P4/free doxorubicin ( $1 \text{ } \mu\text{M}$  doxorubicin/ $23 \text{ } \mu\text{g mL}^{-1}$  nanoparticle) for 48 h, incubated with Hoechst 33 342 at  $5 \text{ } \mu\text{g mL}^{-1}$  for 10 min, and washed with warm PBS and preserved with 4% PFA in sterile PBS prior to imaging with a TCS SPE Leica confocal microscope. For the cytotoxicity assays, corning 7007 ultra-low attachment (ULA) 96-well round bottom plates were used to culture the 3D spheroids. MDA-MB-231 monolayer cells at 80% confluence were detached, collected, and their number determined using a Biorad TC20 automated cell counter. Cell suspensions were diluted in culture medium with the addition of Cultrex basement membrane extract (Cultrex-BME,  $100 \text{ } \mu\text{g mL}^{-1}$ ) and cells were seeded at 1000 cells per well to generate spheroids (final volume of cell suspension in each well was  $100 \text{ } \mu\text{L}$ ). The plates were centrifuged at 300 RCF for 5 min and cultured for 3 days until spheroid formation was confirmed by visual inspection. For dosing, doxorubicin and P4 were prepared as solutions in media and added ( $100 \text{ } \mu\text{L}$ ) at concentrations of  $1 \text{ } \mu\text{M}$  (doxorubicin) and  $1 \text{ } \mu\text{M}$  equivalent doxorubicin ( $23 \text{ } \mu\text{g mL}^{-1}$  P4 nanoparticles) to wells containing a single spheroid in  $100 \text{ } \mu\text{L}$  of medium (making the total volume  $200 \text{ } \mu\text{L}$ ). The plates were imaged, then incubated for 72 h with images taken every day for 3 subsequent days. Spheroid volume analysis, from images obtained with a Nikon Ti Eclipse inverted microscope, utilized an open source macro for the Fiji distribution of ImageJ written by Ivanov.<sup>[31]</sup> The measured area ( $S$ ) from the macro data of a 2D projection of the spheroid was used to calculate the radius, ( $r = \sqrt{\frac{S}{\pi}}$ ) and subsequently, the volume, ( $V = \frac{4}{3}\pi r^3$ ) of an equivalent sphere.

The metabolic activity of cells from the spheroids was measured, as a proxy of cell viability, after 72 h post treatment of the spheroids using an AlamarBlue Cell Viability assay. In these experiments, an aliquot ( $100 \text{ } \mu\text{L}$ ) of cell culture medium was removed from each well and replaced with  $100 \text{ } \mu\text{L}$  10% (v/v) AlamarBlue reagent. The contents of the plate were mixed vigorously for 5 min to destroy the spheroid structure, and the plate was incubated for 4, prior to measurement of fluorescence using a Tecan plate reader at an excitation/emission of 530–560/590 nm.

**In Vivo Studies:** In vivo biodistribution experiments were performed in tumor naïve animals in order to assess distribution, organ accumulation, and clearance of Cy5-labelled pHPMAs of different architectures. The experiments were conducted under the UK Home Office Licence number PPL P435A9CF8. LASA good practice guidelines, FELASA working group on pain and distress guidelines and ARRIVE reporting guidelines were also followed.

Eighteen 8–9 week old female immunodeficient CD-1 NuNu mice were purchased from Charles River UK. Mice were maintained in individually ventilated cages (Tecniplast UK) within a barriered unit, illuminated by fluorescent lights set to give a 12 h light–dark cycle (on 07.00, off 19.00), as recommended in the guidelines to the Home Office Animals (Scientific Procedures) Act 1986 (UK). The room was air-conditioned by a system designed to maintain an air temperature range of  $21 \pm 2 \text{ }^\circ\text{C}$  and a humidity of  $55\% \pm 10\%$ . Mice were housed in social groups, 3 per cage, during the study, with irradiated bedding and autoclaved nesting materials and environmental enrichment (Datesand UK). Sterile irradiated 5V5R rodent diet (IPS Ltd, UK) and autoclaved water was offered ad libitum. The condition of the animals was monitored throughout the study by an experienced animal technician. After a week's acclimatization, the mice were randomly allocated by weight to the study groups of 6 mice per polymer type. As this was a simple biodistribution study, no power calculation was required.

After warming the mice in a thermostatically controlled heating box (Datesand UK), they were injected intravenously via the tail vein with

$100 \text{ } \mu\text{L}$  of a  $500 \text{ } \mu\text{M}$  solution of the selected polymer type in PBS. No adverse effects were observed following the injections or for the duration of the study. The concentration delivered was determined from a balance of non-toxicity from in vitro analysis as well as sufficient fluorescent intensity for imaging in vivo. Prior to the study time points, the mice were anaesthetized with an injectable anesthetic combination (Anaestemine [ketamine]/Sedastart [medetomidine], Animalcare Ltd. UK) before being placed in the imaging system. Images were taken at 1, 4, and 24 h post-injection, and two mice in each group were culled by cervical dislocation, organs were dissected out and were imaged ex vivo at these time points, with the other mice being allowed to recover from the anesthetic with appropriate post procedural monitoring and therapy, including placing mice on a heat pad and providing fluid replacement via wet mash once awake. The organs excized and imaged were the kidneys, liver, spleen, pancreas, lung, heart, bladder, brain, and lymph nodes (subiliac). A urine sample ( $25 \text{ } \mu\text{L}$ ) was also collected and imaged.

For the orthotopic tumor assay, the following protocol was employed. Sixty 6–7 week old female immunodeficient CD-1 NuNu mice were purchased from Charles River UK and maintained as above. After a week's acclimatization, the mice were initiated with tumors as follows:

MDA-MB-231 fLuc cells with viability of  $>90\%$  were re-suspended in growth factor reduced matrigel at  $2 \times 10^6/100 \text{ } \mu\text{L}$  and injected into the left mammary fat pad just inferior to the nipple. Tumor establishment and growth was monitored during the experiment by 2D optical imaging, carried out under anesthesia in the IVIS Spectrum weekly, and were also measured by Vernier calipers (CamLab) twice weekly and animals were weighed weekly. Dosing commenced on day 17 when the tumors had reached a suitable size as established by caliper measurement and bioluminescent imaging, average diameters around 6 mm.

Animals were randomized by volume and bioluminescence intensity, with group numbers of 10 mice per group being arrived at by power calculations as described in the Supporting Information (Figure S9, Supporting Information, ESI).

Injections for the efficacy study were carried out on days 1, 3, 5, 8, 10, 12 by the intravenous route. As above, a thermostatically controlled heating box (Datesand UK) was used to warm the mice, after which they were injected via the tail vein with a solution ( $100 \text{ } \mu\text{L}$ ,  $500 \text{ } \mu\text{M}$ ), of the selected polymer in PBS. No adverse effects were observed following the injections or for the duration of the study. Imaging was carried out weekly as follows: The mice were anaesthetized with an injectable anesthetic combination (Anaestemine [ketamine]/Sedastart [medetomidine], Animalcare Ltd. UK) before being placed in the imaging system. At the pre-determined scientific end point, animals were culled by cervical dislocation, tissues were dissected out and were imaged ex vivo. The tissues excized and imaged were the tumor, kidneys, liver, spleen, pancreas, lung, heart, bladder, brain, and lymph nodes (subiliac). A urine sample ( $25 \text{ } \mu\text{L}$ ) was also collected and imaged. In addition, the tumor, spleen, and heart were weighed prior to preservation. All organs were preserved by snap freezing and fixation (NBF) 50:50.

All images were collected using the IVIS spectrum imaging system, PerkinElmer (MA, USA) and fluorescent signals were quantified using regions of interest and quantified as photons emitted using Living Image/Igor Pro Software (Caliper Life Sciences).

**H&E Staining:** Tumor sections were de-waxed twice in xylene and rinsed twice in ethanol. The sections were then rinsed in tap water, incubated with hematoxylin stain, and subsequently rinsed under tap water. The sections were destained in acidified alcohol and rinsed in tap water again. For the eosin staining, the sections were incubated in eosin and rinsed in tap water, prior to dehydration in alcohol solutions and a final cleaning stage in xylene. The glass coverslips were allowed to dry overnight before recording of micrographs. The mean percentages of positively stained cells were recorded from 20 image fields of view taken at random from the sections.

**Statistical Analysis:** Except where stated, otherwise, in the individual experimental methods sections above, each in vitro experiment was performed three times in triplicate. The statistical analyses of data were performed using analysis of variance (one-way ANOVA) followed by Sidak's post hoc test for multiple comparisons, and the results were presented as

the mean  $\pm$  SD. Statistical significance was accepted at a level of  $p < 0.05$ . ( $*p < 0.05$ ;  $**p < 0.01$ ;  $***p < 0.001$ ;  $****p < 0.0001$ ). GraphPad Prism software (v7.03) was used for statistical analysis.

For the in vivo experiments, values obtained were analyzed using one-way ANOVA followed by Dunnett's test for multiple comparisons, and the data presented as the mean  $\pm$  SD. In all cases, differences were considered significant when  $p^{***} < 0.001$ ,  $p^{**} < 0.01$ , and  $p^* < 0.05$ .

## Supporting Information

Supporting Information is available from the Wiley Online Library or from the author.

## Acknowledgements

V.T., T.F.A., and R.J.C. contributed equally to this work. This work was supported by the Engineering and Physical Sciences Research Council [grant numbers EP/N006615/1; EP/N03371X/1; EP/H005625/1; EP/L013835/1; EP/R035563/1]. This work was also funded by the Royal Society [Wolfson Research Merit Award WM150086] to CA. The authors would also like to thank Douglas Crackett and Paul Cooling for expert technical assistance and Carol Turrill for outstanding administrative support. Histological analysis was performed by the Translational Research team, Cellular Pathology, Nottingham University Hospitals (NUH) Trust and with the assistance of Mr. Dorman Osei.

## Conflict of Interest

The authors declare no conflict of interest.

## Keywords

drug delivery, polymer pro-drugs, polymer therapeutics, self-assembled nanoparticles, triple negative breast cancer

Received: May 5, 2020

Revised: July 7, 2020

Published online: August 2, 2020

- [1] a) J. P. Cadahía, V. Previtali, N. S. Troelsen, M. H. Clausen, *MedChemComm* **2019**, *10*, 1531; b) V. Delplace, P. Couvreur, J. Nicolas, *Polym. Chem.* **2014**, *5*, 1529; c) A. C. Mendes, A. N. Zelikin, *Adv. Funct. Mater.* **2014**, *24*, 5202; d) G. Saravanakumar, J. Kim, W. J. Kim, *Adv. Sci.* **2017**, *4*, 1600124; e) X. D. Ma, E. Ozliseli, Y. Z. Zhang, G. Q. Pan, D. Q. Wang, H. B. Zhang, *Biomater. Sci.* **2019**, *7*, 634; f) J. J. Sun, Y. H. Liu, Y. C. Chen, W. C. Zhao, Q. Y. Zhai, S. Rathod, Y. X. Huang, S. Q. Tang, Y. T. Kwon, C. Fernandez, R. Venkataramanan, S. Li, *J. Controlled Release* **2017**, *258*, 43; g) L. Zheng, Y. Wang, X. Zhang, L. Ma, B. Wang, X. Ji, H. Wei, *Bioconjugate Chem.* **2017**, *29*, 190.
- [2] a) Y.-H. Chien, K. K. Chan, T. Anderson, K. V. Kong, B. K. Ng, K.-T. Yong, *Adv. Ther.* **2019**, *2*, 1800090; b) R. Ferrari, M. Sponchioni, M. Morbidelli, D. Moscatelli, *Nanoscale* **2018**, *10*, 22701; c) A. C. Obermeyer, B. D. Olsen, *ACS Macro Lett.* **2015**, *4*, 101; d) S. A. Elkassih, P. Kos, H. Xiong, D. J. Siegwart, *Biomater. Sci.* **2019**, *7*, 607; e) B. Sui, C. Cheng, P. Xu, *Adv. Ther.* **2019**, *2*, 1900062; f) M. J. Austin, A. M. Rosales, *Biomater. Sci.* **2019**, *7*, 490; g) P. Ray, L. Alhalhooly, A. Ghosh, Y. Choi, S. Banerjee, S. Mallik, S. Banerjee, M. Quadir, *ACS Biomater. Sci. Eng.* **2019**, *5*, 1354; h) J. Deng, F. Liu, L. N. Wang, Y. An, M. Gao, Z. Wang, Y. J. Zhao, *Biomater. Sci.* **2019**, *7*, 429.
- [3] a) M. E. Werner, N. D. Cummings, M. Sethi, E. C. Wang, R. Sukumar, D. T. Moore, A. Z. Wang, *Int. J. Radiat. Oncol., Biol., Phys.* **2013**, *86*, 463; b) K. Sakai-Kato, N. Nishiyama, M. Kozaki, T. Nakanishi, Y. Matsuda, M. Hirano, H. Hanada, S. Hisada, H. Onodera, H. Harashima, Y. Matsumura, K. Kataoka, Y. Goda, H. Okuda, T. Kawanishi, *J. Controlled Release* **2015**, *210*, 76.
- [4] a) J. Rickerby, R. Prabhakar, A. Patel, J. Knowles, S. Brocchini, *J. Controlled Release* **2005**, *101*, 21; b) H. Cabral, K. Miyata, K. Osada, K. Kataoka, *Chem. Rev.* **2018**, *118*, 6844.
- [5] a) H. Baabur-Cohen, L. I. Vossen, H. R. Kruger, A. Eldar-Boock, E. Yeini, N. Landa-Rouben, G. Tiram, S. Wedepohl, E. Markovsky, J. Leor, M. Calderon, R. Satchi-Fainaro, *J. Controlled Release* **2017**, *257*, 118; b) D. Polyak, A. Eldar-Boock, H. Baabur-Cohen, R. Satchi-Fainaro, *Polym. Adv. Technol.* **2013**, *24*, 777.
- [6] G. Shim, M. G. Kim, D. Kim, J. Y. Park, Y. K. Oh, *Adv. Drug Delivery Rev.* **2017**, *115*, 57.
- [7] H. S. Leong, K. S. Butler, C. J. Brinker, M. Azzawi, S. Conlan, C. Dufés, A. Owen, S. Rannard, C. Scott, C. Chen, M. A. Dobrovolskaia, S. V. Kozlov, A. Prina-Mello, R. Schmid, P. Wick, F. Caputo, P. Boisseau, R. M. Crist, S. E. McNeil, B. Fadeel, L. Tran, S. F. Hansen, N. B. Hartmann, L. P. W. Clausen, L. M. Skjolding, A. Baun, M. Ågerstrand, Z. Gu, D. A. Lamprou, C. Hoskins, et al., *Nat. Nanotechnol.* **2019**, *14*, 629.
- [8] S. Wilhelm, A. J. Tavares, Q. Dai, S. Ohta, J. Audet, H. F. Dvorak, W. C. W. Chan, *Nat. Rev. Mater.* **2016**, *1*, 16014.
- [9] a) R. M. England, J. I. Hare, J. Barnes, J. Wilson, A. Smith, N. Strittmatter, P. D. Kemmitt, M. J. Waring, S. T. Barry, C. Alexander, M. B. Ashford, *J. Controlled Release* **2017**, *247*, 73; b) Y. Kaneda, Y. Tsutsumi, Y. Yoshioka, H. Kamada, Y. Yamamoto, H. Kodaira, S. Tsunoda, T. Okamoto, Y. Mukai, H. Shibata, S. Nakagawa, T. Mayumi, *Biomaterials* **2004**, *25*, 3259.
- [10] a) M. Gulfam, T. Matini, P. F. Monteiro, R. Riva, H. Collins, K. Spriggs, S. M. Howdle, C. Jerome, C. Alexander, *Biomater. Sci.* **2017**, *5*, 532; b) J. D. Sadowsky, T. H. Pillow, J. H. Chen, F. Fan, C. R. He, Y. L. Wang, G. Yan, H. Yao, Z. J. Xu, S. Martin, D. L. Zhang, P. Chu, J. dela Cruz-Chuh, A. O'Donohue, G. M. Li, G. D. Rosario, J. T. He, L. N. Liu, C. Ng, D. A. Su, G. D. L. Phillips, K. R. Kozak, S. F. Yu, K. Y. Xu, D. Leipold, J. Wai, *Bioconjugate Chem.* **2017**, *28*, 2086; c) Z.-H. Zhang, Y.-X. Ding, Y.-J. Li, P. Wu, J. Guo, C.-C. Wang, *Adv. Ther.* **2019**, *2*, 1800113; d) S. Zhu, Z. Gu, Y. Zhao, *Adv. Ther.* **2018**, *1*, 1800050.
- [11] C. Conte, F. Mastrotto, V. Taresco, A. Tchoryk, F. Quaglia, S. Stolnik, C. Alexander, *J. Controlled Release* **2018**, *277*, 126.
- [12] T.-Y. Kim, D.-W. Kim, J.-Y. Chung, S. G. Shin, S.-C. Kim, D. S. Heo, N. K. Kim, Y.-J. Bang, *Clin. Cancer Res.* **2004**, *10*, 3708.
- [13] C. E. Vasey, A. K. Pearce, F. Sodano, R. Cavanagh, T. Abelha, V. C. Crucitti, A. B. Anane-Adjei, M. Ashford, P. Gellert, V. Taresco, C. Alexander, *Biomater. Sci.* **2019**, *7*, 3832.
- [14] a) P. Boyle, *Ann. Oncol.* **2012**, *23*, vi7; b) J. Crown, J. O'Shaughnessy, G. Gullo, *Ann. Oncol.* **2012**, *23*, vi56; c) B. P. Schneider, E. P. Winer, W. D. Foulkes, J. Garber, C. M. Perou, A. Richardson, G. W. Sledge, L. A. Carey, *Clin. Cancer Res.* **2008**, *14*, 8010; d) J. J. Arroyo-Crespo, A. Armifian, D. Charbonnier, C. Deladriere, M. Palomino-Schatzlein, R. Lamas-Domingo, J. Forteza, A. Pinedalucena, M. J. Vicent, *Int. J. Cancer* **2019**, *145*, 2267; e) A. Armiñán, M. Palomino-Schatzlein, C. Deladriere, J. J. Arroyo-Crespo, S. Vicente-Ruiz, M. J. Vicent, A. Pinedalucena, *Biomaterials* **2018**, *162*, 144.
- [15] a) H. B. Zhang, W. G. Cui, X. M. Qu, H. Y. Wu, L. L. Qu, X. Zhang, E. Makila, J. Salonen, Y. Q. Zhu, Z. Yang, D. Chen, H. A. Santos, M. T. Hai, D. A. Weitz, *Proc. Natl. Acad. Sci. U. S. A.* **2019**, *116*, 7744; b) J. F. Ji, F. Ma, H. B. Zhang, F. Y. Liu, J. He, W. L. Li, T. T. Xie, D. N. Zhong, T. T. Zhang, M. Tian, H. Zhang, H. A. Santos, M. Zhou, *Adv. Funct. Mater.* **2018**, *28*, 1801738; c) Y. Ashraf, H. Mansouri, V. Laurent-Matha, L. B. Alcaraz, P. Roger, S. Guiu, D. Derocq, G. Robin, H.-A. Michaud, H. Delpech, M. Jarlier, M. Pugnière, B. Robert, A. Puel, L.

- Martin, F. Landomiel, T. Bourquard, O. Achour, I. Fruitier-Arnaudin, A. Pichard, E. Deshayes, A. Turtoi, A. Poupon, J. Simony-Lafontaine, F. Boissière-Michot, N. Pirot, F. Bernex, W. Jacot, S. du Manoir, C. Theillet, et al., *J. ImmunoTher. Cancer* **2019**, *7*, 29; d) G. Palma, C. Conte, A. Barbieri, S. Bimonte, A. Luciano, D. Rea, F. Ungaro, P. Tirino, F. Quaglia, C. Arra, *Int. J. Pharm.* **2014**, *473*, 55.
- [16] a) Z. Wu, A. Shah, N. Patel, X. Yuan, *Bioorg. Med. Chem. Lett.* **2010**, *20*, 5108; b) N. Vale, A. Ferreira, J. Matos, P. Fresco, M. J. Gouveia, *Molecules* **2018**, *23*, 2318; c) Y.-h. Yang, H. Aloysius, D. Inoyama, Y. Chen, L.-q. Hu, *Acta Pharm. Sin. B* **2011**, *1*, 143; d) F. M. de Groot, L. W. van Berkomp, H. W. Scheeren, *J. Med. Chem.* **2000**, *43*, 3093.
- [17] C. D. Walkey, J. B. Olsen, H. B. Guo, A. Emili, W. C. W. Chan, *J. Am. Chem. Soc.* **2012**, *134*, 2139.
- [18] N. Bertrand, P. Grenier, M. Mahmoudi, E. M. Lima, E. A. Appel, F. Dormont, J.-M. Lim, R. Karnik, R. Langer, O. C. Farokhzad, *Nat. Commun.* **2017**, *8*, 777.
- [19] L. Sasso, L. Purdie, A. M. Grabowska, A. T. Jones, C. Alexander, *J. Interdiscip. Nanomed.* **2018**, *3*, 67.
- [20] A. M. Bannunah, D. Vllasaliu, J. Lord, S. Stolnik, *Mol. Pharm.* **2014**, *11*, 4363.
- [21] F. Sodano, R. J. Cavanagh, A. K. Pearce, L. Lazzarato, B. Rolando, A. Fraix, T. F. Abelha, C. E. Vasey, C. Alexander, V. Taresco, S. Sortino, *Biomater. Sci.* **2020**, *8*, 1329.
- [22] A. Tchoryk, V. Taresco, R. H. Argent, M. Ashford, P. R. Gellert, S. Stolnik, A. Grabowska, M. C. Garnett, *Bioconjugate Chem.* **2019**, *30*, 1371.
- [23] A. Ghosh, S. Sarkar, S. Banerjee, F. Behbod, O. Tawfik, D. McGregor, S. Graff, S. K. Banerjee, *PLoS One* **2018**, *13*, e0198143.
- [24] N. Zhao, M. C. Woodle, A. J. Mixson, *J. Nanomed. Nanotechnol.* **2018**, *09*, 519.
- [25] V. J. Venditto, F. C. Szoka Jr., *Adv. Drug Delivery Rev.* **2013**, *65*, 80.
- [26] A. S. Nunes, A. S. Barros, E. C. Costa, A. F. Moreira, I. J. Correia, *Biotechnol. Bioeng.* **2019**, *116*, 206.
- [27] S. Sindhwani, A. M. Syed, J. Ngai, B. R. Kingston, L. Maiorino, J. Rothschild, P. MacMillan, Y. Zhang, N. U. Rajesh, T. Hoang, J. L. Y. Wu, S. Wilhelm, A. Zilman, S. Gadde, A. Sulaiman, B. Ouyang, Z. Lin, L. Wang, M. Egeblad, W. C. W. Chan, *Nat. Mater.* **2020**, *19*, 566.
- [28] S. K. Golombek, J.-N. May, B. Theek, L. Appold, N. Drude, F. Kiessling, T. Lammers, *Adv. Drug Delivery Rev.* **2018**, *130*, 17.
- [29] M. A. Dobrovolskaia, *J. Controlled Release* **2015**, *220*, 571.
- [30] F. Schlenk, S. Werner, M. Rabel, F. Jacobs, C. Bergemann, J. H. Clement, D. Fischer, *Arch. Toxicol.* **2017**, *91*, 3271.
- [31] D. P. Ivanov, T. L. Parker, D. A. Walker, C. Alexander, M. B. Ashford, P. R. Gellert, M. C. Garnett, *PLoS One* **2014**, *9*, e103817.